J. Fluid Mech. (2013), *vol.* 737, *pp.* 412–439.
doi:10.1017/jfm.2013.524

Precession-driven flows in non-axisymmetric ellipsoids

J. Noir† and D. Cébron

Institut für Geophysik, ETH Zürich, Sonneggstrasse 5, Zürich CH-8092, Switzerland

(Received 3 July 2013; revised 23 September 2013; accepted 26 September 2013;
first published online 26 November 2013)

We study the flow forced by precession in rigid non-axisymmetric ellipsoidal containers. To do so, we revisit the inviscid and viscous analytical models that have been previously developed for the spheroidal geometry by, respectively, Poincaré (*Bull. Astronomique*, vol. XXVIII, 1910, pp. 1–36) and Busse (*J. Fluid Mech.*, vol. 33, 1968, pp. 739–751), and we report the first numerical simulations of flows in such a geometry. In strong contrast with axisymmetric spheroids, where the forced flow is systematically stationary in the precessing frame, we show that the forced flow is unsteady and periodic. Comparisons of the numerical simulations with the proposed theoretical model show excellent agreement for both axisymmetric and non-axisymmetric containers. Finally, since the studied configuration corresponds to a tidally locked celestial body such as the Earth's Moon, we use our model to investigate the challenging but planetary-relevant limit of very small Ekman numbers and the particular case of our Moon.

Key words: geophysical and geological flows, topographic effects, wave in rotating fluids

1. Introduction

1.1. *General context*

A rotating rigid object is said to precess when its rotation axis itself rotates about a secondary axis that is fixed in an inertial frame of reference. The case of a precessing fluid-filled container has been studied for over a century because of its multiple applications. These flows are indeed present in fluid-filled spinning tops (Stewartson 1959), gyroscopes (Gans 1984) or the tanks of spacecraft (Garg, Furumoto & Vanyo 1986; Agrawal 1993), possibly affecting the spacecraft's stability (Bao & Pascal 1997). Precession-driven flows are also present in planetary fluid layers, such as the liquid core of the Earth (Greff-Lefftz & Legros 1999) or the Moon (Meyer & Wisdom 2011), where they possibly participate in the dynamo mechanism generating their magnetic fields (Bullard 1949; Bondi & Lyttleton 1953; Malkus 1968). These flows may also have an astrophysical relevance, for instance in the interiors of neutron stars, where they may play a role in the observed precession of radio pulsars (Glampedakis, Andersson & Jones 2009).

The first theoretical studies considered the case of an inviscid fluid in a spheroidal container (Hough 1895; Sloudsky 1895; Poincaré 1910). Assuming a uniform vorticity,

† Email address for correspondence: jerome.noir@erdw.ethz.ch

they obtained a solution, the so-called Poincaré flow, given by the sum of a solid-body rotation and a potential flow. However, the Poincaré solution is modified by the appearance of boundary layers, and some strong internal shear layers are also created in the bulk of the flow (Stewartson & Roberts 1963; Busse 1968). These viscous effects have been taken into account as a correction to the inviscid flow in a spheroid, by considering carefully the Ekman layer and its critical regions (Busse 1968; Zhang, Chan & Liao 2010). Beyond this correction approach, the complete viscous solution, including the fine description of all the flow viscous layers, has recently been obtained in the particular case of a spherical container with weak precession (Kida 2011).

When the precession forcing is large enough compared to viscous effects, instabilities can occur and destabilize the Poincaré flow. First, the Ekman layers can be destabilized (Lorenzani 2001) through standard Ekman layer instabilities (Faller 1991; Lingwood 1997). In this case, the instability remains localized near the boundaries. Second, the whole Poincaré flow can be destabilized, leading to a volume turbulence: this is the precessional instability (Malkus 1968). This small-scale intermittent flow confirms the possible relevance of precession for energy dissipation or magnetic field generation, and has thus motivated many studies. Early experimental attempts (Vanyo 1991; Vanyo *et al.* 1995) to confirm the theory of Busse (1968) did not give very good results (Pais & Le Mouël 2001). Simulations have thus been performed in spherical containers (Tilgner 1999; Tilgner & Busse 2001), spheres (Noir, Jault & Cardin 2001) and finally in spheroidal containers (Lorenzani & Tilgner 2001, 2003), allowing a validation of the theory of Busse (1968). Experimental confirmation of the theory has then been obtained in spheroids (Noir *et al.* 2003), a work followed by many experimental studies involving spheres (Goto *et al.* 2007; Kida & Nakazawa 2010; Boisson *et al.* 2012), spherical containers (Triana, Zimmerman & Lathrop 2012) and also cylinders (Meunier *et al.* 2008; Lagrange *et al.* 2008, 2011).

Finally, the dynamo capability of precession-driven flows has then been demonstrated in spheres (Tilgner 2005, 2007), spheroids (Wu & Roberts 2009) and cylinders (Nore *et al.* 2011), allowing the possibility of a precession-driven dynamo in the liquid core of the Earth (Kerswell 1996) or the Moon (Dwyer, Stevenson & Nimmo 2011).

1.2. *Motivations*

All the previously cited works have considered axisymmetric geometries. However, in natural systems, both planetary rotation and gravitational tides deform the celestial body into a triaxial ellipsoid, where the so-called elliptical (or tidal) instability may take place (Lacaze, Le Gal & Le Dizès 2004; Cébron *et al.* 2010*a*; Le Bars *et al.* 2010). Generally speaking, the elliptical instability can be seen as the inherent local instability of elliptical streamlines (Bayly 1986; Waleffe 1990; Le Dizès 2000), or as the parametric resonance between two free inertial waves (respectively, modes) of the rotating unbounded (respectively, bounded) fluid and an elliptical strain (of azimuthal wavenumber $m = 2$). Similarly, it has been suggested that the precession instability comes from the parametric resonance of two inertial waves with the forcing related to the precession of azimuthal wavenumber $m = 1$ in spheroids (Kerswell 1993; Wu & Roberts 2009) and in cylinders (Lagrange *et al.* 2008, 2011). However, the precession instability is also observed in spheres where there is no $m = 1$ forcing from the container boundary. It has thus been suggested that the precession instability may be related to another mechanism (Lorenzani & Tilgner 2001, 2003). Clearly, the precise

origin of the precession instability is still under debate, and is beyond the scope of the present work. But since tides and precession are simultaneously present in natural systems, it seems necessary to study their reciprocal influence, in the presence or not of instabilities.

The full problem is thus rather complex, involving non-axisymmetric geometries and three different rotating frames: the precessing frame, with a period $T_p \approx 26\,000$ years for the Earth; the frame of the tidal bulge, with a period around $T_d \approx 27$ days for the Earth; and the container or 'mantle' frame, with a period $T_s = 23.9$ hours for the Earth. Working in a frame where the geometry is at rest is particularly suitable for theoretical and numerical studies. The case $T_d = T_p$, where the container is fixed in the precessing frame, has already been considered (Cébron, Le Bars & Meunier 2010*b*), with triaxial ellipsoidal (deformable) containers, in order to study the interaction between the elliptical instability and the precession. In this work, we rather focus on the case $T_d = T_s$, which corresponds to rigid precessing containers. This model is thus relevant for fluid layers of terrestrial planets or moons locked in a synchronization state (i.e. $T_d = T_s$) such as the liquid core of the Moon.

The paper is organized as follows. In § 2, we define the problem and introduce the theoretical inviscid and viscous models considered in this work. Using nonlinear viscous three-dimensional (3D) simulations, we then validate successfully in § 3 the proposed theoretical viscous model. The results obtained are then discussed (§ 4) and applied to the liquid core of the Moon in the conclusion (§ 5).

2. Mathematical description of the problem

We consider an incompressible fluid of density ρ and kinematic viscosity ν enclosed in a triaxial ellipsoid of principal axes (a, b, c). The cavity rotates along its principal axis of length c, and precesses along the unit vector $\hat{\boldsymbol{k}}_p$, as illustrated in figure 1(*a*). We denote by $\boldsymbol{\Omega}_m$ the instantaneous total vector of rotation of the cavity in the inertial frame, by $\boldsymbol{\Omega_o} = \Omega_o \hat{\boldsymbol{k}}$ the rotation vector of the cavity in the precessing frame, and by $\boldsymbol{\Omega_p} = \Omega_p \hat{\boldsymbol{k}}_p$ the precession vector in the inertial frame, such that

$$\boldsymbol{\Omega}_m = \boldsymbol{\Omega_o} + \boldsymbol{\Omega_p}. \tag{2.1}$$

2.1. *Frames of reference*

In figure 1, we represent the ellipsoidal cavity and the different vectors in the three frames of reference of interest for the present study. In the inertial frame (figure 1*a*), the precession vector is fixed, and the cavity rotates around the time-dependent vector $\hat{\boldsymbol{k}}(t)$, which describes a precessional motion around $\hat{\boldsymbol{k}}_p$. In the frame of precession (figure 1*b*), both $\hat{\boldsymbol{k}}$ and $\hat{\boldsymbol{k}}_p$ are fixed, and the cavity rotates around $\hat{\boldsymbol{k}}$ (the orientation of the principal axis of the cavity varies in time). In the body frame attached to the cavity (figure 1*c*), the orientations of the principal axes are fixed, and the precession vector $\hat{\boldsymbol{k}}_p(t)$ exhibits a retrograde motion around $\hat{\boldsymbol{k}}$.

2.2. *Coordinate systems*

We define two systems of coordinates (figure 2): $(\hat{\boldsymbol{X}}_m, \hat{\boldsymbol{Y}}_m, \hat{\boldsymbol{Z}}_m)$, attached to the ellipsoid and oriented along its principal axes (a, b, c); and $(\hat{\boldsymbol{X}}_p, \hat{\boldsymbol{Y}}_p, \hat{\boldsymbol{Z}}_p)$, attached to the precessing frame. In the rotating frame attached to the principal axes of the ellipsoid, the unit vectors $\hat{\boldsymbol{X}}_p$ and $\hat{\boldsymbol{Y}}_p$ rotate in a retrograde direction. We define the

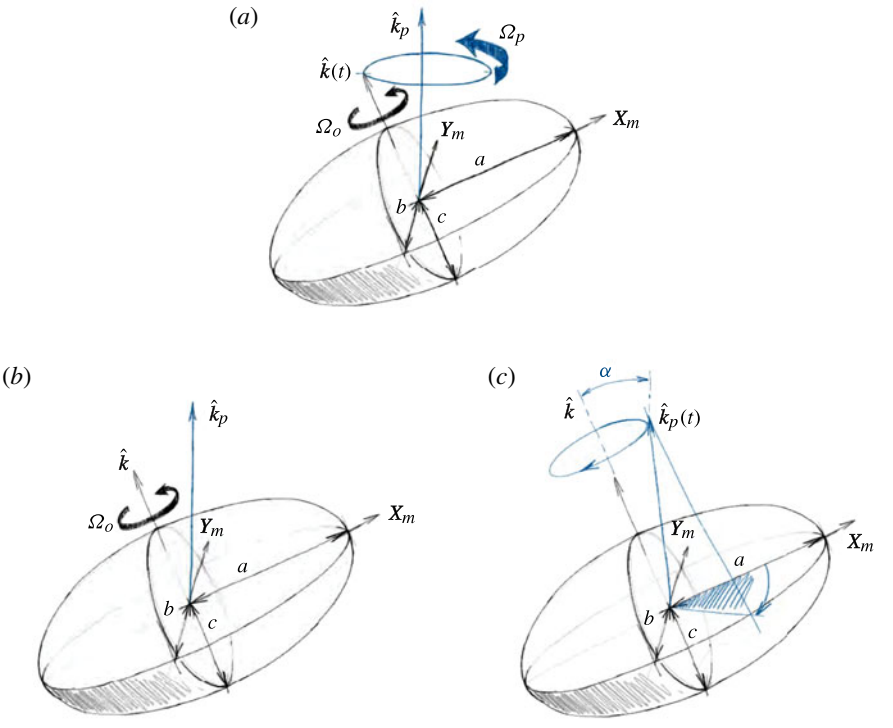

FIGURE 1. (Colour online) Schematic representation of the precessing ellipsoidal cavity, as seen from the three frames of reference: (*a*) the inertial frame, (*b*) the frame of precession and (*c*) the body frame.

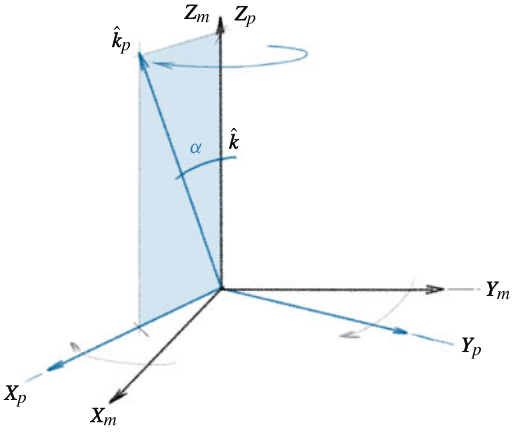

FIGURE 2. (Colour online) The coordinate systems: $(\boldsymbol{X}_m, \boldsymbol{Y}_m, \boldsymbol{Z}_m)$ is attached to the body and oriented along the principal axes (a, b, c) of the ellipsoid. In contrast, $(\boldsymbol{X}_p, \boldsymbol{Y}_p, \boldsymbol{Z}_p)$ is attached to the precessing frame.

time origin such that, at $t = 0$, $\hat{\boldsymbol{X}}_p = \hat{\boldsymbol{X}}_m$ and $\hat{\boldsymbol{Y}}_p = \hat{\boldsymbol{Y}}_m$. As shown in figure 2, $\hat{\boldsymbol{Z}}_p = \hat{\boldsymbol{Z}}_m$ at all times.

If we consider an arbitrary vector $\boldsymbol{A}$ of coordinates (x_p, y_p, z_p) in the coordinate system attached to the precessing frame, its coordinates in the system $(\hat{\boldsymbol{X}}_m, \hat{\boldsymbol{Y}}_m, \hat{\boldsymbol{Z}}_m)$ are given by

$$x_m = x_p \cos(\Omega_o t) + y_p \sin(\Omega_o t), \tag{2.2a}$$

$$y_m = -x_p \sin(\Omega_o t) + y_p \cos(\Omega_o t), \tag{2.2b}$$

$$z_m = z_p. \tag{2.2c}$$

In the frame of reference attached to the moving body, the equation of the triaxial ellipsoid boundary is given by

$$\frac{x^2}{a^2} + \frac{y^2}{b^2} + \frac{z^2}{c^2} = 1. \tag{2.3}$$

In the present study, we will mostly consider two types of geometries: an axisymmetric spheroid ($a = b \neq c$), which we refer to as a spheroid; and a biaxial ellipsoid ($a \neq b = c$), which we refer to as a non-axisymmetric ellipsoid. The true ellipsoidal geometry ($a \neq b \neq c$) will be referred to as a triaxial ellipsoid, but will only be considered to derive the general inviscid equations, the fundamental dynamics due to a non-axisymmetric equator being already captured when ($a \neq b = c$). The reduced tensor of inertia expressed in the coordinate system attached to the principal axes of the cavity reads

$$I = \frac{4\pi}{15} \begin{bmatrix} b^2 + c^2 & 0 & 0 \\ 0 & a^2 + c^2 & 0 \\ 0 & 0 & b^2 + a^2 \end{bmatrix}. \tag{2.4}$$

2.3. *Fluid equations of motion*

Without further assumptions, the fluid motion inside the precessing ellipsoid is governed by the nonlinear Navier–Stokes equation. Using Ω_o^{-1} as a time scale and $R = (abc)^{1/3}$ as a length scale, any velocity field $\boldsymbol{u}$ within the precessing ellipsoid is governed by the following equations, expressed in the body frame:

$$\frac{\partial \boldsymbol{u}}{\partial t} + 2(\hat{\boldsymbol{k}} + Po\,\hat{\boldsymbol{k}}_p) \times \boldsymbol{u} + \boldsymbol{u} \cdot \boldsymbol{\nabla} \boldsymbol{u} = -\boldsymbol{\nabla} p - Po(\hat{\boldsymbol{k}}_p \times \hat{\boldsymbol{k}}) \times \boldsymbol{r} + E\,\Delta \boldsymbol{u}, \tag{2.5}$$

$$\boldsymbol{\nabla} \cdot \boldsymbol{u} = 0, \tag{2.6}$$

where p is the reduced pressure, which takes the centrifugal force into account, $Po = \Omega_p / \Omega_o$ is the so-called Poincaré number and $E = \nu / (\Omega_o R^2)$ is the Ekman number, which represents the relative amplitude of the viscous and Coriolis forces.

If the fluid is viscous, the boundary condition is

$$\boldsymbol{u} = \boldsymbol{0}, \tag{2.7}$$

which reduces to

$$\boldsymbol{u} \cdot \boldsymbol{n} = 0 \tag{2.8}$$

for an inviscid fluid ($E = 0$), with $\boldsymbol{n}$ the unit vector normal to the boundary surface.

Finally, we introduce the Rossby number, which combines the rate of precession Po and the angle of precession α. It is a measure of the amplitude of the forcing:

$$Ro = Po\|\hat{\boldsymbol{k}}_p \times \hat{\boldsymbol{k}}\| = Po\sin\alpha. \tag{2.9}$$

In previous studies, the angle of precession α was fixed and the Poincaré number was varied, and so the Rossby number varies also. In this study, we fix the Rossby number, $Ro = 10^{-2}$, to ensure that the flow remains stable in our simulations, even at the largest values of Po. Consequently, the angle of precession varies as $\sin\alpha = Ro/Po$ as we scan in Po. It follows that there is a forbidden band $-10^{-2} < Po < 10^{-2}$ for which no α can satisfy (2.9). The same study could be carried out at fixed α by varying the Poincaré number. The same conclusions would apply as long as no instability develops in the system. This means that there would be a forbidden zone depending on the critical values of Po, which we do not know. Note, finally, that to access the small-Po region of the parameter space, one could simply reduce Ro accordingly.

2.4. *Inviscid flows of uniform vorticity in triaxial precessing ellipsoids*

Following the earlier work of Hough (1895), Sloudsky (1895) and Poincaré (1910), we assume the fluid to be inviscid and search for a solution of the velocity that is linear in the spatial coordinates (x, y, z), i.e. a particular solution $\boldsymbol{U}$ of uniform vorticity

$$\boldsymbol{U} = \boldsymbol{\omega} \times \boldsymbol{r} + \boldsymbol{\nabla}\psi, \tag{2.10}$$

where $\boldsymbol{\omega}$ is the mean rotation component of the flow and $\boldsymbol{\nabla}\psi$ is the gradient flow needed to satisfy the non-penetration boundary condition. It is straightforward to show that such a solution does not generate any viscous force in the interior, which is consistent with our assumption.

Taking the curl of the Navier–Stokes equations (2.5) in the body frame, we obtain the vorticity equation for the particular flow (2.10):

$$\frac{\partial\boldsymbol{\omega}}{\partial t} = (\boldsymbol{\omega} + Po\,\hat{\boldsymbol{k}}_p(t) + \hat{\boldsymbol{k}}) \cdot \boldsymbol{\nabla}\boldsymbol{U} - Po\,\hat{\boldsymbol{k}}_p(t) \times \hat{\boldsymbol{k}}. \tag{2.11}$$

An important step to establish the general equation for the mean vorticity is to express $\boldsymbol{U}$, or equivalently ψ, as a function of $(\omega, a, b, c, x, y, z)$. This can be done by imposing the non-penetration condition on the velocity together with the condition of incompressibility, but this is rather lengthy. Instead, we propose to follow an approach similar to that in the original work of Poincaré (1910).

First, we introduce a geometrical transformation that applies in the body frame where the ellipsoid is fixed and that transforms the triaxial cavity (a, b, c) into a sphere with unit radius (see figure 3). Using a prime to denote quantities in the spherical domain and no prime for quantities in the true ellipsoid, we have

$$x \to x' = x/a, \quad y \to y' = y/b, \quad z \to z' = z/c. \tag{2.12}$$

The velocity is transformed following the same rules:

$$u_x \to u'_x = u_x/a, \quad u_y \to u'_y = u_y/b, \quad u_z \to u'_z = u_z/c. \tag{2.13}$$

It is easy to show that the fluid in the spherical domain remains incompressible, of uniform vorticity and does not penetrate the boundary. Note, however, that it does not satisfy the 'no-slip' nor the 'stress-free' boundary conditions. Therefore, it can only be a solution of the inviscid Euler equation (Tilgner 1998). We now make use of

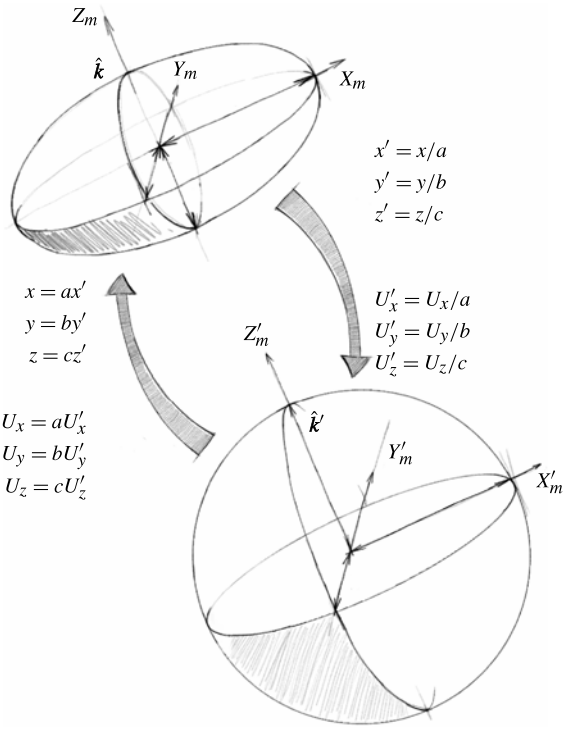

FIGURE 3. Schematic representation of the geometrical stretch that transforms a triaxial ellipsoid into a sphere of radius unity.

this transformation and its reciprocal to easily obtain the analytical expression of the uniform vorticity flow in the body frame of the true ellipsoid.

In the spherical domain, a flow of uniform vorticity simply takes the form of a solid-body rotation:

$$\boldsymbol{U}' = \boldsymbol{\omega}' \times \boldsymbol{r}' = (\omega'_y z' - \omega'_z y', \omega'_z x' - \omega'_x z', \omega'_x y' - \omega'_y x'). \tag{2.14}$$

Substituting (2.12) and (2.13) into (2.14) leads to

$$\boldsymbol{U} = \left(\omega'_y \frac{a}{c} z - \omega'_z \frac{a}{b} y, \omega'_z \frac{b}{a} x - \omega'_x \frac{b}{c} z, \omega'_x \frac{c}{b} y - \omega'_y \frac{c}{a} x\right) \tag{2.15}$$

Since $\boldsymbol{\omega}'$ is a uniform vector field, the mean vorticity in the ellipsoid is

$$\boldsymbol{\nabla} \times \boldsymbol{U} = \left(\omega'_x \left(\frac{c}{b} + \frac{b}{c}\right), \omega'_y \left(\frac{a}{c} + \frac{c}{a}\right), \omega'_z \left(\frac{b}{a} + \frac{a}{b}\right)\right) = 2\boldsymbol{\omega}. \tag{2.16}$$

From (2.15) and (2.16), we finally obtain the analytical form of uniform vorticity inviscid flows in triaxial ellipsoids:

$$U_x = \omega_y \frac{2a^2}{a^2 + c^2} z - \omega_z \frac{2a^2}{a^2 + b^2} y, \tag{2.17a}$$

$$U_y = \omega_z \frac{2b^2}{a^2 + b^2} x - \omega_x \frac{2b^2}{c^2 + b^2} z, \tag{2.17b}$$

$$U_z = \omega_x \frac{2c^2}{b^2+c^2} y - \omega_y \frac{2c^2}{a^2+c^2} x. \tag{2.17c}$$

Identifying the terms within (2.10), we obtain the expression for the potential field ψ:

$$\psi = \omega_x \frac{c^2-b^2}{c^2+b^2} yz + \omega_y \frac{a^2-c^2}{a^2+c^2} xz + \omega_z \frac{b^2-a^2}{b^2+a^2} xy. \tag{2.18}$$

Anticipating the rest of the paper, we introduce $\boldsymbol{\Omega}$, the space-averaged rotation vector of the fluid in the precessing frame:

$$\boldsymbol{\Omega} = \boldsymbol{\omega} + \hat{\boldsymbol{k}}. \tag{2.19}$$

Using the coordinate system attached to the principal axes of the ellipsoid, we obtain from (2.2)

$$\omega_x = \Omega_x \cos(t) + \Omega_y \sin(t), \tag{2.20a}$$

$$\omega_y = -\Omega_x \sin(t) + \Omega_y \cos(t), \tag{2.20b}$$

$$\omega_z = \Omega_z - 1. \tag{2.20c}$$

Substituting the analytical expression of the velocity (2.17) in the vorticity equation (2.11), we obtain the general form of the equations that govern the inviscid solution of uniform vorticity in the body frame for a precessing triaxial ellipsoid:

$$\frac{\partial \omega_x}{\partial t} = 2a^2 \left[\frac{1}{a^2+c^2} - \frac{1}{a^2+b^2}\right] \omega_z \omega_y + P_x \sin(t) \frac{2a^2}{a^2+b^2} \omega_z + (P_z+1) \frac{2a^2}{a^2+c^2} \omega_y + P_x \sin(t), \tag{2.21}$$

$$\frac{\partial \omega_y}{\partial t} = 2b^2 \left[\frac{1}{a^2+b^2} - \frac{1}{b^2+c^2}\right] \omega_x \omega_z + P_x \cos(t) \frac{2b^2}{a^2+b^2} \omega_z - (P_z+1) \frac{2b^2}{b^2+c^2} \omega_x + P_x \cos(t), \tag{2.22}$$

$$\frac{\partial \omega_z}{\partial t} = 2c^2 \left[\frac{1}{b^2+c^2} - \frac{1}{a^2+c^2}\right] \omega_x \omega_y - P_x \cos(t) \frac{2c^2}{a^2+c^2} \omega_y - P_x \sin(t) \frac{2c^2}{b^2+c^2} \omega_x, \tag{2.23}$$

with $P_x = Po \sin\alpha = Ro$ and $P_z = Po \cos\alpha = Po\sqrt{Ro^2 - Po^2}$. These equations are valid for any values of (a, b, c), Po and α. In a spheroidal cavity, there exist an infinite number of stationary solutions for the system (2.21)–(2.23) given by

$$\boldsymbol{\omega} + \hat{\boldsymbol{k}} = \xi \hat{\boldsymbol{k}}_p, \tag{2.24}$$

where ξ can be any real number. Among this class of inviscid solutions, only the solution $\xi = -Po$ remains stationary when $a \neq b$, for all c.

2.5. *Reintroducing the viscosity*

Without viscous damping, the inviscid solutions depend on the initial conditions and are somewhat of limited interest. Assuming the Ekman number to be small, we reintroduce the viscosity through the viscous torque due to the friction in the Ekman boundary layer.

In the Appendix, we extend the approach of Noir *et al.* (2003) for a spheroid to the case of finite ellipticity. Without any loss of generality, the viscous equations (2.21)–(2.23) can be written as

$$\frac{\partial \omega_x}{\partial t} = \left[\frac{2a^2}{a^2+c^2} - \frac{2a^2}{a^2+b^2}\right]\omega_z\omega_y + P_x\sin(t)\frac{2a^2}{a^2+b^2}\omega_z + (P_z+1)\frac{2a^2}{a^2+c^2}\omega_y + P_x\sin(t) + \mathscr{L}\boldsymbol{\Gamma}_v|_x, \tag{2.25}$$

$$\frac{\partial \omega_y}{\partial t} = \left[\frac{2b^2}{a^2+b^2} - \frac{2b^2}{b^2+c^2}\right]\omega_x\omega_z + P_x\cos(t)\frac{2b^2}{a^2+b^2}\omega_z - (P_z+1)\frac{2b^2}{b^2+c^2}\omega_x + P_x\cos(t) + \mathscr{L}\boldsymbol{\Gamma}_v|_y, \tag{2.26}$$

$$\frac{\partial \omega_z}{\partial t} = \left[\frac{2c^2}{b^2+c^2} - \frac{2c^2}{a^2+c^2}\right]\omega_x\omega_y - P_x\cos(t)\frac{2c^2}{a^2+c^2}\omega_y - P_x\sin(t)\frac{2c^2}{b^2+c^2}\omega_x + \mathscr{L}\boldsymbol{\Gamma}_v|_z. \tag{2.27}$$

Using the linear asymptotic of spin-up and of the spin-over mode, we derive an analytical expression of the viscous term in the limit of small Ekman number:

$$\mathscr{L}\boldsymbol{\Gamma}_v = \sqrt{E\Omega}\left[\frac{\lambda^r_{so}}{\Omega^2}\begin{pmatrix}\Omega_x\Omega_z\\ \Omega_y\Omega_z\\ \Omega_z^2-\Omega^2\end{pmatrix} + \frac{\lambda^i_{so}}{\Omega}\begin{pmatrix}\Omega_y\\ -\Omega_x\\ 0\end{pmatrix} + \lambda_{sup}\frac{\Omega^2-\Omega_z}{\Omega^2}\begin{pmatrix}\Omega_x\\ \Omega_y\\ \Omega_z\end{pmatrix}\right], \tag{2.28}$$

where λ^r_{so} and λ^i_{so} represent the decay rate and the viscous correction to the eigenfrequency of the spin-over mode, respectively. In the context of spheroids of finite ellipticity, we use the asymptotic values derived by Zhang, Liao & Earnshaw (2004). In addition, λ_{sup} is an integrated value of the spin-up decay rate and is derived from the asymptotic theory of Greenspan (1968). We refer to this form of the viscous term as the generalized model in the rest of the paper

In the case of a non-axisymmetric container, no analytical solution for the inertial modes exists. Lacking a proper theory for the viscous damping of inertial modes in a non-axisymmetric container, we adopt the following reduced form for the viscous torque:

$$\mathscr{L}\boldsymbol{\Gamma}_v = \lambda\sqrt{E}\begin{pmatrix}\Omega_x\\ \Omega_y\\ \Omega_z-1\end{pmatrix}. \tag{2.29}$$

In § A.2, we show that, for an axisymmetric container, the viscous term (2.28) is well approximated by the reduced form (2.29) in the range of parameters considered in this study. Hence, λ can be interpreted as an approximation of the decay rate λ^r_{so} of the spin-over mode when the contribution from the terms proportional to λ^i_{so} and λ_{sup} are negligible. In the absence of a model of the spin-over mode in a non-axisymmetric ellipsoid, λ in our model remains an adjustable parameter and is determined so as to best fit the numerical results in each geometry. Herein, we refer to the viscous set of equations using (2.29) as the reduced model.

Anticipating the rest of the paper, we introduce the reduced viscous equations in the frame of precession for the particular class of ellipsoid ($a \neq b = c$). Substituting (2.2) into the inviscid set of equations (2.25)–(2.27) with $b = c$, we obtain

$$\frac{\partial \Omega_x}{\partial t} = P_z\Omega_y + (1-\chi)\left[\cos(2t)\left(\frac{P_z+2}{2}\Omega_y - \frac{1}{2}\Omega_y\Omega_z\right) + \sin(2t)\left(-\frac{P_z+2}{2}\Omega_x + P_x\Omega_z + \frac{1}{2}\Omega_x\Omega_z - P_x\right) + \frac{P_z}{2}\Omega_y + \frac{1}{2}\Omega_y\Omega_z\right] + \lambda\sqrt{E}\Omega_x, \tag{2.30}$$

$$\frac{\partial \Omega_y}{\partial t} = P_x\Omega_z - P_z\Omega_x + (1-\chi)\left[\cos(2t)\left(\frac{P_z+2}{2}\Omega_x - \frac{1}{2}\Omega_x\Omega_z - P_x\Omega_z + P_x\right) + \sin(2t)\left(\frac{P_z+2}{2}\Omega_y - \frac{1}{2}\Omega_y\Omega_z\right) - \frac{P_z}{2}\Omega_x - \frac{1}{2}\Omega_x\Omega_z\right] + \lambda\sqrt{E}\Omega_y, \tag{2.31}$$

$$\frac{\partial \Omega_z}{\partial t} = -P_x\Omega_y + (1-\chi)\left[\cos(2t)\left(\frac{P_x}{2}\Omega_y + \Omega_x\Omega_y\right) + \sin(2t)\left(-\frac{P_x}{2}\Omega_x + \frac{1}{2}\left(\Omega_y^2 - \Omega_x^2\right)\right) + \frac{P_x}{2}\Omega_y\right] + \lambda\sqrt{E}(\Omega_z - 1), \tag{2.32}$$

with the ratio χ of the two equatorial moments of inertia given by

$$\chi = \frac{b^2+c^2}{a^2+b^2} = \frac{2b^2}{a^2+b^2}. \tag{2.33}$$

3. Comparison of the theoretical models with numerical simulations

To allow for an easy comparison with previous studies, we will focus our diagnostic on two quantities: the rotation vector of the fluid viewed from the frame of precession, $(\Omega_x, \Omega_y, \Omega_z)$; and the amplitude of the differential angular velocity between the fluid and the surrounding container, $\|\boldsymbol{\Omega} - \hat{\boldsymbol{k}}\|$.

3.1. *Methods*

The system of ordinary differential equations describing the time evolution of the uniform vorticity components of the flow, i.e. (2.25)–(2.27), is solved using the Dormand–Prince method, the standard version of the Runge–Kutta algorithm implemented in MATLAB. We have checked that the time evolution is not modified by the use of other time stepping solvers.

The system of partial differential equations of the initial viscous problem, i.e. the equations of motion (2.5) and (2.6) completed by the boundary condition (2.7) at the ellipsoid surface, is solved using a finite element method implemented in the commercial code COMSOL Multiphysics. The mesh element type used for the fluid variables is the standard Lagrange element $P1 - P2$, which is linear for the pressure field and quadratic for the velocity field. For time stepping, we use the implicit differential-algebraic (IDA) solver, based on variable-coefficient backward differencing formulas (BDF) (see Hindmarsh *et al.* (2005) for details on the IDA solver). The integration method in IDA is of variable order, the order ranging between 1 and 5. At each time step the system is solved with the sparse direct linear solver

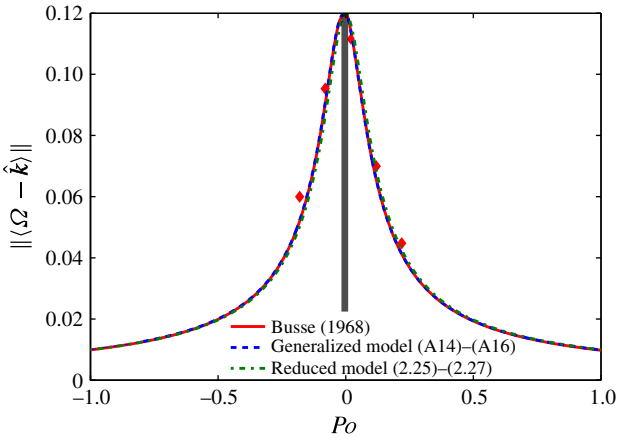

FIGURE 4. (Colour online) Equatorial component of the fluid mean rotation as a function of the Poincaré number in a spherical geometry. The numerical simulations are performed with $E = 10^{-3}$ and $Ro = 10^{-2}$. The diamond symbols (red online) represent the simulations; The various line strokes represents the different models as indicated. The vertical line symbolizes the region of the parameter space $|Po| < 10^{-2}$ where no α can satisfy $Ro = Po \sin\alpha$.

PARDISO (www.pardiso-project.org). All computations have been performed on a single workstation.

Since we are concerned with the effect of topography in our system, we have chosen to fix the Ekman number, $E = 10^{-3}$, which allows us to use meshes with typically 30 000 degrees of freedom. Convergence tests in a spherical geometry have been performed to ensure that our simulations with this resolution capture correctly the viscous effects due to the Ekman boundary layer. Figure 4 represents the norm of differential rotation between the fluid and the container in a spherical geometry, $\|\boldsymbol{\Omega} - \hat{\boldsymbol{k}}\|$. The diamond symbols (red online) represent the numerical simulations, the red solid line represents the asymptotic solution of Busse (1968), the blue dashed line represents the generalized model (A 14)–(A 16) and the green dot-dashed line represents the reduced model. The best fit leads to $\lambda = -2.62$. We observe a quantitative agreement between all the models and the numerical simulations. A close look at the critical Po shows that the reduced model predicts a resonance at zero while the generalized model and Busse's theory predict a resonance at $Po \sim -0.01$. This difference is consistent with the fact that the reduced model does not account for the viscous correction of the eigenfrequency of the Poincaré mode, which at these parameters is of order 0.01.

In the present study we are concerned with the flow component of uniform vorticity. In the simulations, the uniform vorticity is obtained by averaging the fluid vorticity at each time step over a volume inside an ellipsoid:

$$\frac{x^2}{a^2} + \frac{y^2}{b^2} + \frac{z^2}{c^2} = d^2, \tag{3.1}$$

with $d = 1 - 5\sqrt{E}$ to exclude the Ekman boundary layer (see also Cébron *et al.* 2010*b*).

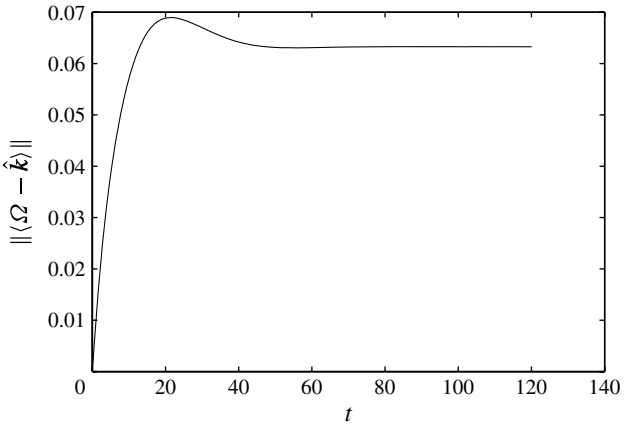

FIGURE 5. Time evolution of the amplitude of the equatorial component of rotation of the fluid in the frame of precession from the simulations: $a = b = 1$, $c = 0.5$, $E = 10^{-3}$, $Ro = 10^{-2}$ and $Po = -0.45$.

3.2. *The axisymmetric spheroid, $a = b \neq c$*

In this particular geometry, the reduced model systematically leads to a flow that is steady in the precessing frame.

Figure 5 represents the time evolution of the norm of the differential rotation, $\|\boldsymbol{\Omega} - \hat{\boldsymbol{k}}\|$, from the 3D nonlinear simulations ($a = b = 1$, $c = 0.5$, $E = 10^{-3}$, $Ro = 10^{-2}$ and $Po = -0.45$). It shows that the uniform vorticity component becomes stationary after a typical period of 60 rotations, which is comparable to the spin-up time $t \propto E^{-1/2} \sim 30$. This result is generic to all of our simulations in an axisymmetric spheroid. Hence, it validates the otherwise assumed stationarity of the uniform vorticity solution in the asymptotic theory of Busse (1968) and Noir *et al.* (2003).

Figure 6 shows the differential rotation, $\|\boldsymbol{\Omega} - \hat{\boldsymbol{k}}\|$, for $a = b = 1$ and $c = 0.5,\ 0.8,\ 1.1,\ 1.5$ as we scan in Poincaré numbers from -1 to $+1$. For each geometry, we perform a least-squares inversion using the reduced model to determine the value of λ that best fits the numerical simulations. The results for each value of c are presented in table 1. We choose to study each individual component in the precessing frame where the total vorticity remains time-independent. Figure 7 shows the individual components of $\boldsymbol{\Omega}$ viewed from the precessing frame.

We retrieve the classical result that the amplitude of the differential rotation, $\|\boldsymbol{\Omega} - \hat{\boldsymbol{k}}\|$, exhibits resonant-like peaks for a critical value of the Poincaré number, Po_c. Considering each individual component (figure 7), the peaks correspond to a maximum of Ω_y and a (usually abrupt) change of sign of Ω_x. As we shall see later at lower Ekman number, the term *resonance* may have a significance in the inviscid limit, but for finite viscosity we prefer to use the term *transition* and define Po_c as $\Omega_x(Po_c) = 0$, the transition thus corresponding to the abrupt change of direction of the mean rotation axis of the fluid. Physically, Po_c is the Poincaré number for which the equatorial component of the fluid rotation is exactly aligned with the gyroscopic forcing $\hat{\boldsymbol{k}}_p \times \hat{\boldsymbol{k}}$, leading to a pseudo-resonance between the precessional forcing and the so-called Poincaré mode (see Noir *et al.* (2003) for more details). As expected from the asymptotic and inviscid theory, $Po_c < 0$ for an oblate spheroid, $a > c$, and $Po_c > 0$ for a prolate spheroid, $a < c$.

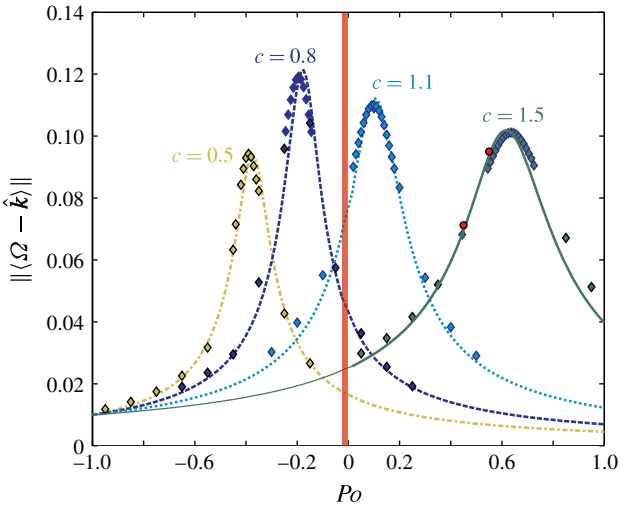

FIGURE 6. (Colour online) Amplitude of differential rotation, $\|\boldsymbol{\Omega} - \hat{\boldsymbol{k}}\|$, as a function of the Poincaré number. The symbols represent our numerical simulations at $E = 10^{-3}$ and $Ro = 10^{-2}$; the curves represent the reduced model with the inverted values of λ from table 1. Each value of the polar axis c is represented by a different line stroke (colour online) as indicated. The vertical line signifies the region of the parameter space $|Po| < 10^{-2}$ where no α can satisfy $Ro = Po \sin\alpha$. The circles (red online) represent simulations with $c = 1.5$ with a spatial resolution four times larger (135 000 degrees of freedom).

c	0.5	0.8	1.1	1.5
λ	−3.35	−2.57	−2.78	−2.97

TABLE 1. Inverted viscous coefficient λ for an axisymmetric spheroid.

Figure 7 shows the components of $\boldsymbol{\Omega}$ (viewed from the frame of precession). We compare the three different models, namely, Busse (1968), the generalized model and the reduced model, to the numerical simulations. Comparing the relative amplitude of the different components, the differential motion is clearly dominated by the equatorial component, which thus governs the evolution of $\|\boldsymbol{\Omega} - \hat{\boldsymbol{k}}\|$ shown in figure 6. We observe a quantitative agreement between the reduced model and the numerical results for Ω_x and Ω_y. The small departure of Ω_z from 1 is less accurately captured by the model, owing to its weak influence on $\|\boldsymbol{\Omega} - \hat{\boldsymbol{k}}\|$, from which we invert for the unique adjustable parameter λ. Meanwhile, the generalized model, without any adjustable parameter, predicts correctly the resonance positions but tends to overestimate the amplitudes as c is increased. One can however note that the results of this predictive model are still acceptable for $c \in [0.5; 1.1]$. In contrast, the usual Busse (1968) model does not predict correctly the flow components' evolution, or even the resonance locations, as soon as the spheroid deformation becomes significant, which is expected given the domain of validity of this model.

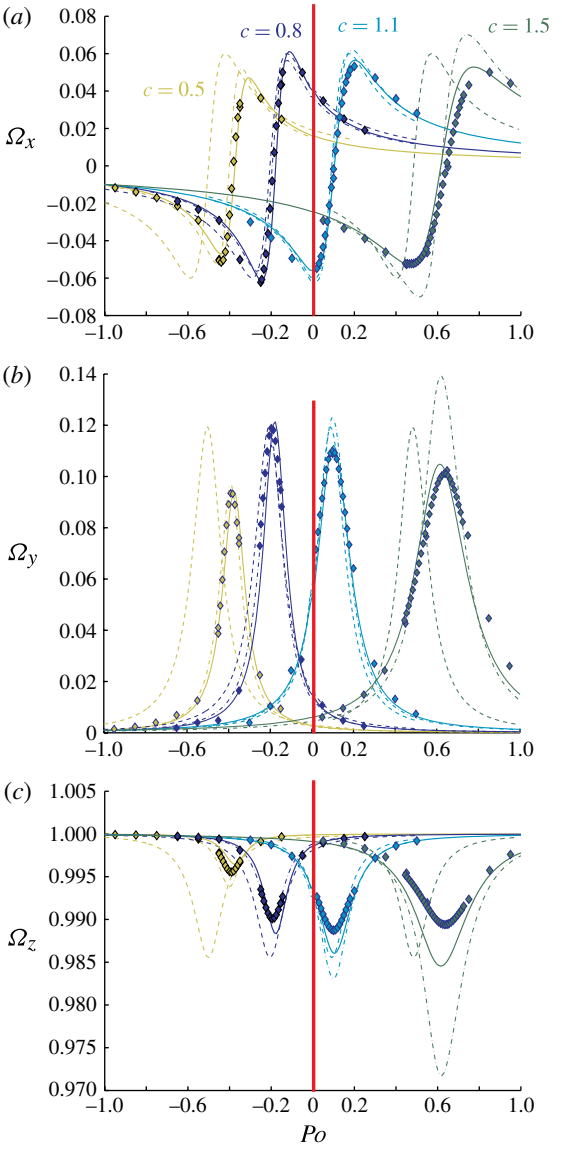

FIGURE 7. (*a–c*) The x, y and z components of the fluid rotation vector in the frame of precession within an axisymmetric spheroid. We compare our simulations (symbols), the theory of Busse (1968) (dashed lines), our generalization of this model (dot-dashed lines) and the proposed reduced model (solid lines) with the inverted values of λ from table 1. Each value of the polar axis c is represented by a different colour as indicated. The vertical line symbolizes the region of the parameter space $|Po| < 10^{-2}$ where no α can satisfy $Ro = Po \sin\alpha$.

3.2.1. *The non-axisymmetric spheroid,* $a \neq b = c = 1$

Figure 8 represents the time evolution of the three components of the fluid rotation vector in the frame of precession from the 3D nonlinear numerical simulations with $a = 0.5$, $b = c = 1$. Comparison with figure 5 shows clearly an important difference: in non-axisymmetric ellipsoids, an unsteady and periodic flow can be forced by the

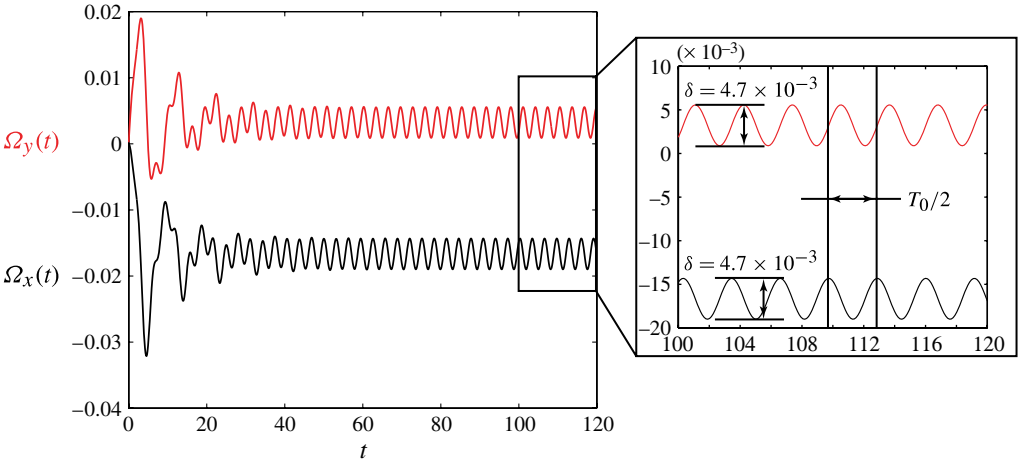

FIGURE 8. (Colour online) Time evolution of the three components of the fluid rotation vector in the frame of precession $\Omega_x(t)$, $\Omega_y(t)$ from the numerical simulations for $a = 0.5$, $b = c = 1$, $E = 10^{-3}$, $Ro = 10^{-2}$ and $Po = -0.45$.

precession, contrary to the flow forced in a spheroid, which is steady. The inset shows moreover that Ω_x and Ω_y oscillate in phase quadrature, with the same amplitude $\delta/2$ and the same period, which is half the container rotation period T_0 (dimensionless value of T_0 is 2π).

Figure 9 represents the same data set as in figure 8 plotted in three dimensions to illustrate the dynamics of the mean rotation vector. The fluid rotation vector performs a time-periodic quasi-circular motion (dotted ellipse; red online) around its mean position (lighter grey arrow; blue online). The semi-aperture angle of the cone is given by $\sqrt{\Omega_x^2 + \Omega_y^2}$.

We carry out a series of 3D numerical simulations for various geometries with $a \neq b = c$. In each case we perform the least-squares inversion to determine λ using only the time-averaged differential rotation, $\|\langle \boldsymbol{\Omega} - \hat{\boldsymbol{k}} \rangle\|$ (figure 10). As in the case of an axisymmetric container, we observe peaks at critical values of the Poincaré number, identical in the mean and oscillatory components. We note that the critical Po is retrograde for $a > 1$ and prograde for $a < 1$, which correlates with the results obtained in an axisymmetric spheroid. Indeed, in any meridional cross-section of the non-axisymmetric cavity, the trace of the boundary is an ellipse with a polar axis shorter than the mean equatorial axis for $a > 1$, similar to an oblate spheroid, and longer than the mean equatorial axis for $a < 1$, similar to a prolate spheroid. As the geometry tends towards the sphere ($a = 1$), the amplitude of the peak of the oscillatory component vanishes, while the peak of the time-averaged component converges towards the solution for the sphere, as illustrated in figure 10.

We observe a quantitative agreement between our reduced model and the numerical simulations for both the mean and oscillatory components for all cases with $a > b = c$. For $a < b = c$, the reduced model captures correctly the dynamics of the time-averaged equatorial rotation but exhibits significant discrepancy in the axial components.

Figure 11 shows the time-averaged and oscillatory components, respectively, of $\boldsymbol{\Omega}$. The steady part of the uniform vorticity behaves as in an axisymmetric container.

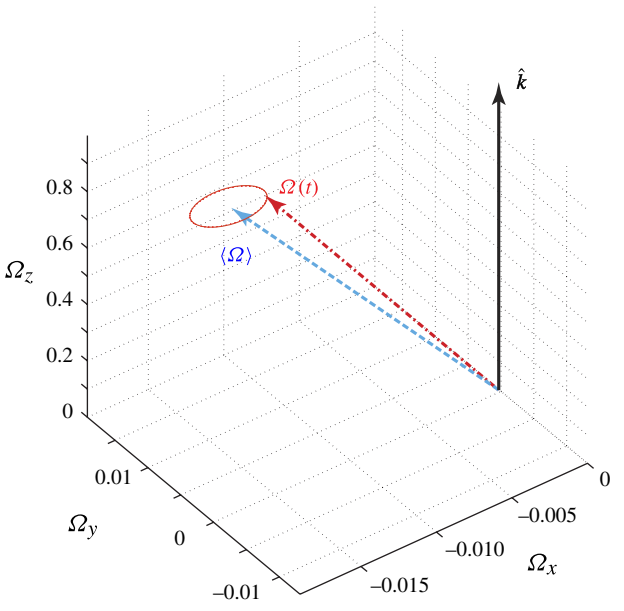

FIGURE 9. (Colour online) Time evolution of the fluid rotation vector $\boldsymbol{\Omega}$ viewed from the frame of precession (same set of parameters as in figure 8). The dashed arrow (blue online) represents the mean rotation vector $\langle\boldsymbol{\Omega}\rangle$; the dot-dashed arrow (red online) represents the instantaneous rotation vector at a particular time; the ellipse (red online) shows the trace of the instantaneous rotation vector for $60 < t < 120$; and the black arrow shows the container rotation vector.

Its axial component Ω_z departs only marginally from the vorticity of the container; hence the differential motion between the fluid and the container is dominated by the equatorial component. Even though we invert for the unique adjustable parameter using the steady part only, we observe a very good agreement between the reduced model and the simulations. All three components exhibit a maximum amplitude at the critical Po_c derived from the time-averaged part. As suggested from the time evolution shown in figure 8, the two equatorial components have the same amplitude; the axial component is only five times smaller. In addition, we note a significant discrepancy in both the peak location and amplitude between the reduced model and the numerical simulations for $a = 0.5$, similarly to the case of a prolate axisymmetric spheroid.

4. Discussion

In the Appendix, we show that the location of Po_c, within an axisymmetric container, is determined primarily by the inviscid part of the equations, while the typical amplitude is most constrained by the decay rate λ^r_{so}. We also note that the viscous correction to the spin-over eigenfrequency accounts for a small shift of Po_c but does not modify the fundamental dynamics, even at the moderate Ekman numbers considered here. Finally, the effect of the non-vanishing axial differential rotation in the frame rotating with the fluid remains negligible in all of our simulations. The systematic mismatch of the amplitude of the generalized model with our simulations is likely to be due to the moderate Ekman numbers accessible in our numerical simulations. Meanwhile, the observed shift in Po_c in figures 7 and 11 shows the

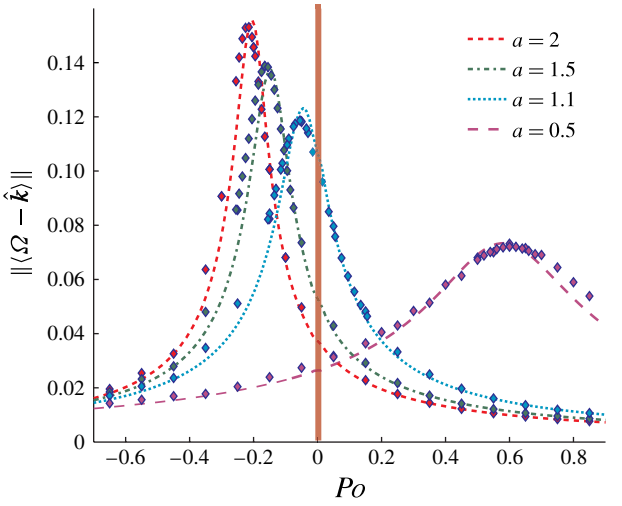

FIGURE 10. (Colour online) Amplitude of the mean differential rotation, $\|\langle \boldsymbol{\Omega} - \hat{\boldsymbol{k}} \rangle\|$, as a function of the Poincaré number. The symbols represent numerical simulations at $E = 10^{-3}$ and $Ro = 10^{-2}$; the curves represent the inverted reduced model. Each geometry, characterized by a, is represented with a different line stroke as indicated. The vertical line symbolizes the region of the parameter space $|Po| < 10^{-2}$ where no α can satisfy $Ro = Po \sin\alpha$.

a	0.5	1.1	1.5	2
λ	-4.5 ± 0.02	-2.54 ± 0.02	-2.29 ± 0.02	-2.03 ± 0.02

TABLE 2. Inverted viscous coefficient λ for a non-axisymmetric spheroid.

limitations of the one adjustable parameter reduced model, which only accounts for part of the dissipation mechanism.

The simulations presented here show that the flow of uniform vorticity in a non-axisymmetric ellipsoid is not purely stationary in the frame of precession as it would be for a spheroidal cavity. This is supported by the governing equations (2.30)–(2.32), from which one can anticipate that, if a stationary uniform vorticity component exists, it will necessarily drive a time-dependent perturbation for $\chi \neq 1$, i.e. when the two equatorial moments of inertia are not equal.

Our results suggest that the simple form of the viscous term (2.29) captures well the fundamental dynamics of the uniform vorticity flow in a non-axisymmetric precessing ellipsoid. Taking advantage of the computational efficiency of this reduced model, we perform a series of time integrations at lower Ekman numbers. Figure 12 shows the norm of the mean and oscillatory components of the differential $\boldsymbol{\Omega} - \hat{\boldsymbol{k}}$ as a function of the Poincaré number for decreasing Ekman numbers in the case $a = 1.5$, $b = c = 1$. We assume the decay rate λ to be independent of the Ekman number and equal to the value inverted in this geometry at $E = 10^{-3}$ (see table 2). As the Ekman number is reduced, both the stationary and the oscillatory parts of the differential rotation tend towards an asymptotic limit already captured at 10^{-7}.

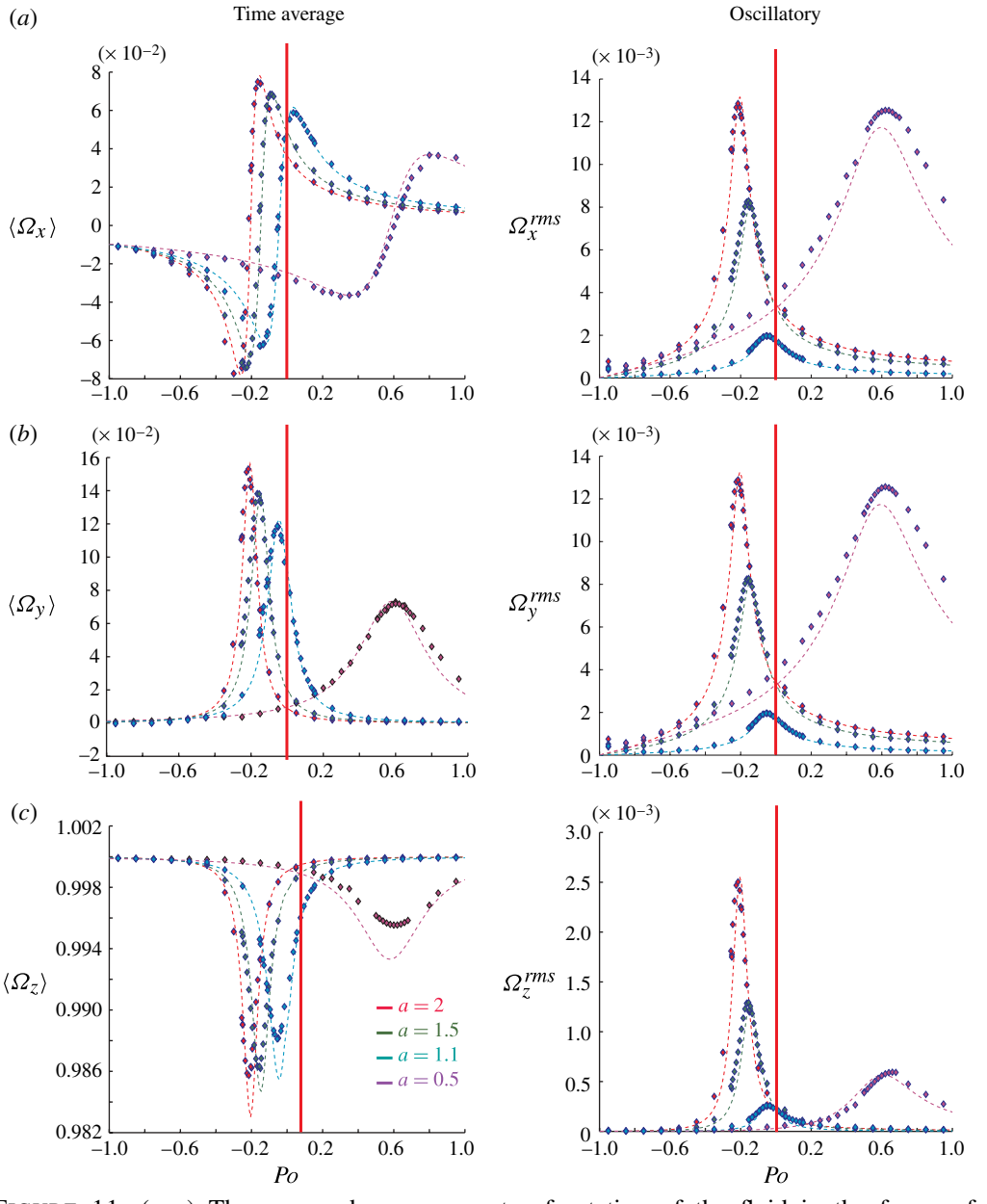

FIGURE 11. (*a–c*) The x, y and z components of rotation of the fluid in the frame of precession. The left column shows the time-averaged components, and the right column shows the time standard deviation of the components. We compare, for each geometry (i.e. a), our simulations (symbols) and the reduced model (dashed lines) with the inverted values of λ from table 2. The vertical line is the region of the parameter space $|Po| < 10^{-2}$ where no α can satisfy $Ro = Po \sin\alpha$.

Let us define the mean longitude ϕ and the mean latitude θ of the fluid rotation axis as follows:

$$\cos\phi = \frac{\langle\Omega_x\rangle}{\sqrt{\langle\Omega_x\rangle^2 + \langle\Omega_y\rangle^2}}, \tag{4.1}$$

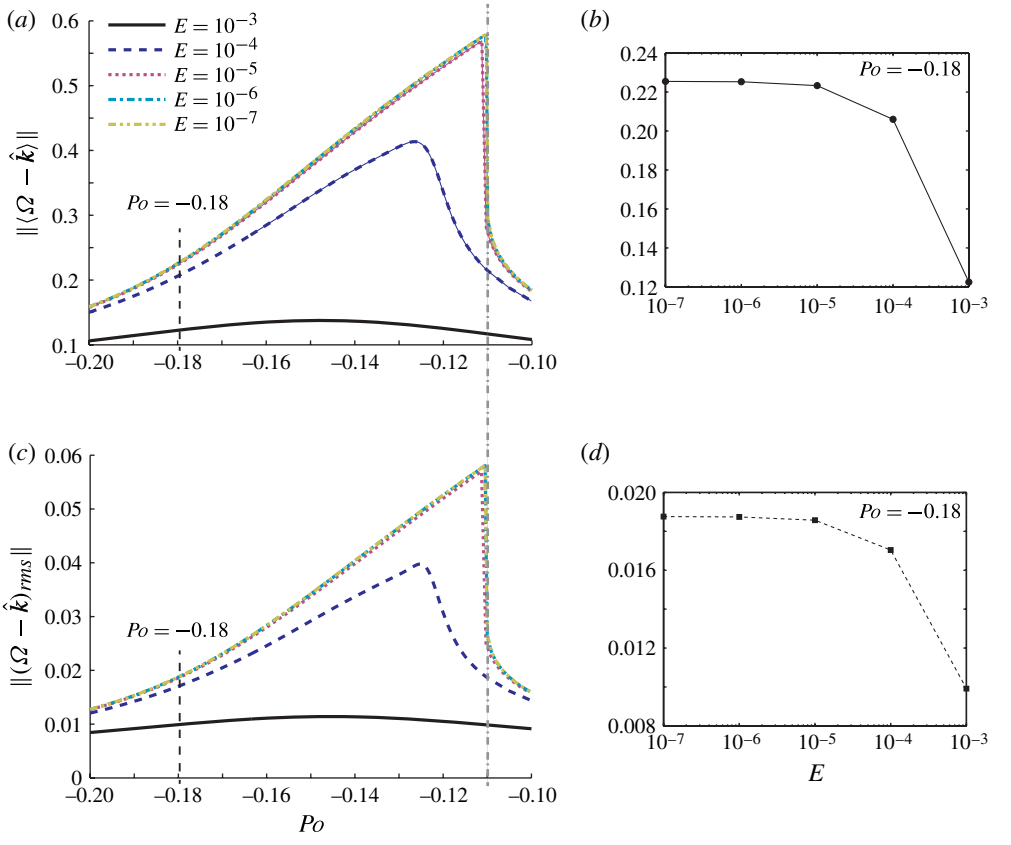

FIGURE 12. (Colour online) Norm of the (*a*) stationary and (*c*) oscillatory components of the differential rotation $\boldsymbol{\omega}$ as a function of the Poincaré number for various Ekman numbers. Norm of the (*b*) stationary and (*d*) oscillatory parts of the differential rotation for a fixed $Po = -0.18$ as a function of the Ekman number. In all calculations we integrate in time the reduced model with $a = 1.5$, $b = c = 1$ and $\lambda = -2.3$.

$$\tan\theta = \frac{\langle\Omega_z\rangle}{\sqrt{\langle\Omega_x\rangle^2 + \langle\Omega_y\rangle^2}}. \tag{4.2}$$

Figure 13 shows the evolution of the longitude and latitude for decreasing Ekman numbers. As for the amplitude, we observe that the direction of the stationary component of uniform vorticity tends towards an asymptotic value. We note that the asymptotic longitude is either 0 or 180°, which corresponds to a fluid mean rotation vector lying in the plane $(\hat{\boldsymbol{k}}, \hat{\boldsymbol{k}}_p)$. Hence, similarly to the case of an axisymmetric spheroid, it is the viscosity that forces the mean rotation vector to leave the plane containing the axis of the container and the axis of precession. In that plane, at vanishing Ekman numbers, the rotation vector evolves from high latitudes ($\boldsymbol{\Omega}$ almost aligned with $\hat{\boldsymbol{k}}$), far from the transition, to mid-latitudes near the transition.

Our results suggest that, at low enough Ekman number, the flow of uniform vorticity driven by the precession of the container becomes independent of E, or, in fact, independent of the viscous term $\lambda\sqrt{E}$. Hence, outside of the transition region, the asymptotic solution for vanishing viscosity can be found using any arbitrary

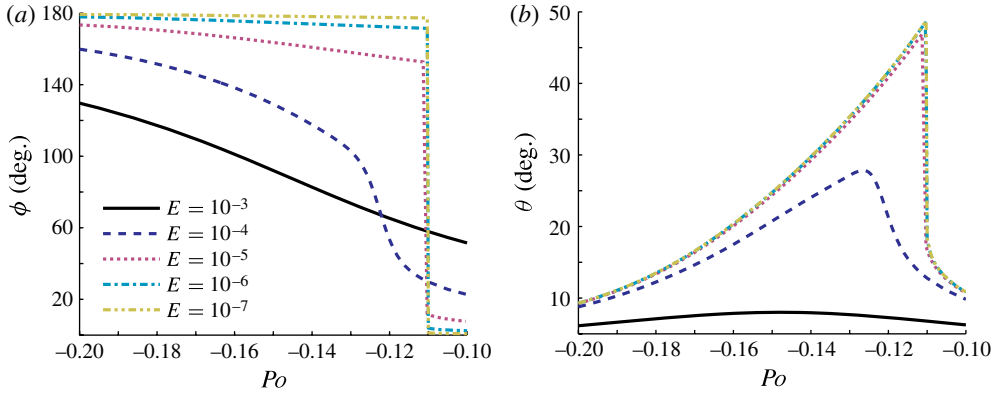

FIGURE 13. (Colour online) (*a*) Longitude and (*b*) latitude of the stationary part of the rotation vector.

order $O(1)$ value of the damping factor, providing that the Ekman number is small enough, typically when $E^{1/2} \lesssim (1-\chi)$.

5. Conclusion

In the present study, we investigate the flow of uniform vorticity driven by precession in a spheroid and a non-axisymmetric ellipsoid. We report the first numerical simulations in a non-axisymmetric ellipsoid showing that, in contrast to a spheroid, the flow of uniform vorticity viewed from the frame of precession is no longer stationary.

In addition, we develop a semi-analytical model first by deriving the inviscid equations and then by reintroducing the viscosity. We propose a generalized model in the case of a spheroid of arbitrary ellipticity following the torque approach introduced by Noir *et al.* (2003) and using the linear asymptotic theory of the spin-over mode as a proxy. For non-axisymmetric ellipsoids an analogous theory has yet to be established, and the same approach is not possible. Nevertheless, we introduce a reduced model with one adjustable parameter that we compare successfully with 3D nonlinear numerical simulation at a fixed Ekman number, $E = 10^{-3}$ (using the commercial software COMSOL).

Despite its simplicity, the reduced model with one adjustable parameter allows us to reproduce quantitatively the uniform vorticity flow obtained from numerical integrations of the full Navier–Stokes equations both in a spheroid and in a non-axisymmetric ellipsoid. Furthermore, the generalized model for a spheroid allows us to extend the classical asymptotic theory of Busse (1968) and Noir *et al.* (2003) to finite ellipticity as is usually the case in laboratory experiments. With our current limited number of geometrical configurations (four different values of a), it is not possible to ascertain the functional relationship between the geometrical deformation and the damping factor.

Taking advantage of the computational efficiency of the reduced model compared to the full simulations of Navier–Stokes equations, we investigate the uniform vorticity flow in non-axisymmetric ellipsoids as the Ekman number is decreased. We show that the uniform vorticity converges towards an asymptotic solution independent of the Ekman number and thus of the viscous term as a whole. At very low Ekman numbers,

$1-\chi$	2.5×10^{-5}	Le Bars *et al.* (2011)
E	$\sim10^{-12}$	Le Bars *et al.* (2011)
Po	-3.9×10^{-3}	Meyer & Wisdom (2011)
α	1.54°	Meyer & Wisdom (2011)

TABLE 3. Dimensionless parameters for the Earth's Moon.

the time-averaged component of the fluid rotation axis lies in the plane formed by the precession and container rotation vectors as in the case of a spheroid, while the time-dependent component tends towards a finite amplitude.

When looking at the dynamics in greater detail, we identify some limitations of our reduced model: first, there is a small shift of the critical value of the Poincaré number at which we observe a transition; and second, the axial component of the fluid rotation exhibits a simpler dynamics in our reduced model than in the numerical simulations.

Owing to the limited range of Ekman numbers accessible in the numerical simulations, we believe that an experimental survey is necessary to complement the results presented in this study. With an experimental set-up using water as a working fluid, a typical length scale $\sqrt{abc}\sim15$ cm and rotating at $\Omega_0\sim240$ r.p.m., the achievable Ekman number will be of order 3×10^{-6}. Aside from testing the validity of the reduced model, it would be suitable to investigate the stability of the flow.

Two recent publications have investigated possible mechanisms to drive the Earth's Moon early dynamo. One invokes a precession-driven turbulence in the liquid core (Dwyer *et al.* 2011), whereas the other proposes a meteoritic impact leading to a desynchronization of the Moon (Le Bars *et al.* 2011). Considering our current tidally locked Moon, the core–mantle boundary (CMB) geometry is close to a non-axisymmetric ellipsoid rather than an axisymmetric spheroid (typically, its shape can be approximated by the well-known relation $(b-c)/(a-c)=1/4$ assuming hydrostatic state and homogeneous material). We can thus compare our reduced model, assumed to be valid for our current Moon, and the model of Busse (1968), which is valid at planetary settings but assumes a spheroidal CMB. The parameters used for the simulation are given in table 3. The reduced model for a non-axisymmetric ellipsoid and the model of Busse (1968) for a spheroid agree within 0.3 %, leading to a mean differential rotation amplitude of the order of 3 % of the planetary rotation rate and a core spin vector normal to the ecliptic plane in agreement with a former model by Goldreich (1967). Neither the viscous nor the pressure torques are large enough to force the lunar core to precess with the mantle. Nevertheless, in contrast with a spheroidal model, the reduced model predicts an unsteady component of uniform vorticity of order $2.3\times10^{-6}\,\Omega_o$ oscillating with a period of $T\approx13.5$ days. Although this amplitude is small, one may question what could happen if, in the frame of precession, there exists another source of gravitational perturbation at that frequency. Indeed, in that case, direct or parametric resonances may occur, leading to much larger amplitude flows, subsequent instabilities, and thus to enhanced dissipation.

Acknowledgements

The first author would like to dedicate this paper to the memory of Roland Leger (1921–2012). The authors would like to thank N. Rambaux for fruitful discussions on the initial work of H. Poincaré, and J. Laskar for the invitation to the Poincaré 100 years anniversary, which led to this study. J.N. is supported by ERC grant 247303

MFECE; D.C. is supported by the ETH Zürich Postdoctoral Fellowship Program as well as by the Marie Curie Actions for People COFUND Program.

Appendix. The viscous torque for a precessing spheroid of arbitrary ellipticity

A.1. *The viscous torque*

In the limit of small ellipticity, small Ekman number and small $Po\sin\alpha$, Busse (1968) and Noir *et al.* (2003) have derived the viscous equations for the stationary flow of uniform vorticity in a precessing axisymmetric spheroid. We herein refer to this model as Busse (1968), who was the first to derive it in the limit of small ellipticity, small Ekman number and small $Po\sin\alpha$. In this appendix, we follow the same approach as Noir *et al.* (2003) to derive a more general model for finite ellipticity.

To reintroduce the viscosity, we assume a small Ekman number such that, at leading order, the uniform vorticity solution in the bulk remains essentially inviscid and the viscous forces are important only in the Ekman boundary layer. The Navier–Stokes equation for an arbitrary viscous flow $\boldsymbol{u}$ in the frame of precession leads to the following torque balance in the precessing frame (within the spheroid volume V):

$$\overbrace{\int_V \boldsymbol{r}\times\frac{\partial \boldsymbol{u}}{\partial t}\,\mathrm{d}V}^{\Gamma_t}+\overbrace{\int_V \boldsymbol{r}\times(\boldsymbol{u}\cdot\boldsymbol{\nabla}\boldsymbol{u})\,\mathrm{d}V}^{\Gamma_{nl}}+\overbrace{2\int_V \boldsymbol{r}\times(\boldsymbol{\Omega}_p\times\boldsymbol{u})\,\mathrm{d}V}^{\Gamma_i}$$
$$=\overbrace{-\int_V \boldsymbol{r}\times\boldsymbol{\nabla}p\,\mathrm{d}V}^{\Gamma_p}+\overbrace{E\int_V \boldsymbol{r}\times\nabla^2\boldsymbol{u}\,\mathrm{d}V}^{\Gamma_v}. \tag{A 1}$$

The challenge is thus to obtain the viscous torque due to the Ekman layer.

As previously, we consider a uniform vorticity flow in a spheroid, which can be seen as a quasi-solid-body rotation along an axis tilted from the container rotation axis. Note that no further assumption is made on the stationarity in the frame of precession. For the particular flow $\boldsymbol{U}=\boldsymbol{\omega}\times\boldsymbol{r}+\boldsymbol{\nabla}\phi$, the integration of $\boldsymbol{\Gamma}_t$, which is carried out in the coordinate system attached to the ellipsoidal container, leads to

$$\mathscr{L}\boldsymbol{\Gamma}_t=\frac{\partial\boldsymbol{\omega}}{\partial t}, \tag{A 2}$$

where $\mathscr{L}$ is the matrix

$$\mathscr{L}=\frac{15}{16\pi}\begin{bmatrix}\dfrac{b^2+c^2}{b^2c^2} & 0 & 0\\ 0 & \dfrac{a^2+c^2}{a^2c^2} & 0\\ 0 & 0 & \dfrac{b^2+a^2}{b^2a^2}\end{bmatrix}. \tag{A 3}$$

The differential rotation between the fluid and the surrounding container in the body frame can be decomposed into an axial and an equatorial component relative to the rotation axis of the fluid:

$$\boldsymbol{\delta\omega}_z=\left(\frac{\boldsymbol{\Omega}-\hat{\boldsymbol{k}}}{\Omega^2}\cdot\boldsymbol{\Omega}\right)\boldsymbol{\Omega}, \tag{A 4}$$

$$\boldsymbol{\delta\omega}_{eq}=\boldsymbol{\Omega}-\hat{\boldsymbol{k}}-\boldsymbol{\delta\omega}_z. \tag{A 5}$$

Without the viscous torque acting on the fluid, the equatorial component would tend to grow a spin-over mode, while the axial component would result in a spin-up or spin-down of the fluid. Thus, following the approach of Noir *et al.* (2003), the viscous torque can be derived from the linear decay rate of Greenspan (1968) for the spin-over and spin-up:

$$\mathscr{L}\boldsymbol{\Gamma}_{\nu}^{eq,z} = \left.\frac{\partial(\boldsymbol{\delta\omega}_{eq,z})}{\partial t}\right|_{t=0}. \tag{A 6}$$

Since the linear calculation is only valid in the frame rotating with the fluid, we introduce a modified Ekman number $E_f = E/\Omega$ and a rescaled time $t_f = \Omega t$ associated with this frame of reference. According to Greenspan (1968), the time evolution of the spin-over mode in the non-rotating frame can be written as (Noir *et al.* 2003)

$$\begin{aligned}\boldsymbol{\delta\omega}_{eq}(t) = \exp(\lambda_{so}^{r}E_f^{1/2}t_f)[&\boldsymbol{\delta\omega}_{eq}(0)\cos(\lambda_{so}^{i}E_f^{1/2}t_f)\\ &- \boldsymbol{\Omega}\times\boldsymbol{\delta\omega}_{eq}(0)\sin(\lambda_{so}^{i}E_f^{1/2}t_f)/\Omega].\end{aligned} \tag{A 7}$$

It follows that

$$\mathscr{L}\boldsymbol{\Gamma}_{\nu}^{eq} = (E\Omega)^{1/2}\left[\frac{\lambda_{so}^{r}}{\Omega^2}\begin{pmatrix}\Omega_x\Omega_z\\ \Omega_y\Omega_z\\ \Omega_z^2-\Omega^2\end{pmatrix} + \frac{\lambda_{so}^{i}}{\Omega}\begin{pmatrix}\Omega_y\\ -\Omega_x\\ 0\end{pmatrix}\right]. \tag{A 8}$$

In contrast with Noir *et al.* (2003), who use λ_{so}^{r} and λ_{so}^{i} in the spherical approximation of Greenspan (1968), we propose to use the analytical prediction of λ_{so}^{r} and λ_{so}^{i} obtained from Zhang *et al.* (2004) in an oblate spheroid ($c < a$) of arbitrary ellipticity. Although the author does not claim that his derivation remains valid in a prolate spheroid ($c > a$), we have checked that the formula reproduces the results of Greenspan (1968) and are thus valid for prolate spheroids. It is important to note that the derivation of the spin-over decay rate is valid only for an axisymmetric container. Then, if the tilt of the fluid rotation axis and the ellipticity is not small enough, the viscous torque in the precessing cavity can no longer be inferred from the axisymmetric spin-over mode asymptotic theory introduced above.

The axial differential rotation can be treated similarly. Without the viscous torque, the axial differential rotation would tend to spin-up or spin-down the fluid. From Greenspan (1968), the time evolution of an axial differential rotation can be written as

$$\boldsymbol{\delta\omega}_z(s,t) = \boldsymbol{\delta\omega}_z(0)[1-\exp(\lambda_{sup}^{*}(s)E_f t_f)], \tag{A 9}$$

with a coefficient $\lambda_{sup}^{*}(s)$ that changes with the cylindrical radius s. An explicit analytical expression for $\lambda_{sup}^{*}(s)$ is given by Greenspan & Howard (1963) for axisymmetric containers, which can be written in the case of a spheroid as

$$\lambda_{sup}^{*}(s) = -\frac{[1-s^2(1-c^2)]^{1/4}}{c\,(1-r^2)^{3/4}}. \tag{A 10}$$

Hence, the axial viscous torque can be estimated as

$$\mathscr{L}\boldsymbol{\Gamma}_{\nu}^{z} = \lambda_{sup}\sqrt{E}\left(1-\frac{\Omega_z}{\Omega^2}\right)\begin{pmatrix}\Omega_x\\ \Omega_y\\ \Omega_z\end{pmatrix}, \tag{A 11}$$

with

$$\lambda_{sup} = \int \lambda^*_{sup}(s)\,\mathrm{d}s = -\frac{\sqrt{\pi^3/2}}{c\Gamma(3/4)^2}\,F([-1/4,\,1/2],\,[3/4],\,1-c^2), \tag{A 12}$$

where Γ is simply the gamma function and $F(n, d, z)$ is the usual generalized hypergeometric function, also known as the Barnes extended hypergeometric function (see, respectively, chapters 6 and 15 of Abramowitz & Stegun 1972). Note that, when the tilt of the fluid mean rotation axis with respect to that of the mantle becomes large, i.e. when the container is no longer axisymmetric from the fluid point of view, we do not expect this derivation of the torque to apply either.

Finally, taking into account both the spin-up and spin-over contributions yields

$$\mathscr{L}\boldsymbol{\Gamma}_v = \sqrt{E\Omega}\left[\frac{\lambda^r_{so}}{\Omega^2}\begin{pmatrix}\Omega_x\Omega_z\\ \Omega_y\Omega_z\\ \Omega_z^2-\Omega^2\end{pmatrix} + \frac{\lambda^i_{so}}{\Omega}\begin{pmatrix}\Omega_y\\ -\Omega_x\\ 0\end{pmatrix} + \lambda_{sup}\frac{\Omega^2-\Omega_z}{\Omega^2}\begin{pmatrix}\Omega_x\\ \Omega_y\\ \Omega_z\end{pmatrix}\right]. \tag{A 13}$$

Substituting (2.2) into (2.25)–(2.27) with $a = b$, we obtain the viscous equations in the frame of precession:

$$\frac{\partial\Omega_x}{\partial t} = P_z\Omega_y - (1-\gamma)[P_z\Omega_y + \Omega_y\Omega_z] + \mathscr{L}\boldsymbol{\Gamma}_v\cdot\hat{\boldsymbol{e}}_x, \tag{A 14}$$

$$\frac{\partial\Omega_y}{\partial t} = P_x\Omega_z - P_z\Omega_x + (1-\gamma)\,[P_z\Omega_x + \Omega_x\Omega_z] + \mathscr{L}\boldsymbol{\Gamma}_v\cdot\hat{\boldsymbol{e}}_y, \tag{A 15}$$

$$\frac{\partial\Omega_z}{\partial t} = -P_x\Omega_y - (1-\gamma)P_x\Omega_y + \mathscr{L}\boldsymbol{\Gamma}_v\cdot\hat{\boldsymbol{e}}_z, \tag{A 16}$$

where $\gamma = (2a^2)/(a^2+c^2)$ represents the ratio of the polar to equatorial moments of inertia.

Taking (A 14) $\times\,\Omega_x$ + (A 15) $\times\,\Omega_y$ + (A 16) $\times\,\Omega_z$ yields

$$(\boldsymbol{\Omega}-\hat{\boldsymbol{k}})\cdot\boldsymbol{\Omega} = \frac{(1-\gamma)P_x\Omega_y\Omega_z}{\lambda_{sup}\sqrt{E}}. \tag{A 17}$$

Then, in the limit $|(1-\gamma)|P_x/\sqrt{E} \ll 1$, we recover the so-called no-spin-up condition introduced by Noir *et al.* (2003), which is also equivalent to the solvability condition of Busse (1968). This condition, also used by Cébron *et al.* (2010*b*), is thus not valid in general for a spheroid of arbitrary ellipticity.

A.2. *Comparison between the different models in an axisymmetric spheroid*

Substituting (2.2) into (2.25)–(2.27) with $a = b$, we obtain the viscous equations in the frame of precession. We thus have three different models for the axisymmetric spheroid: the asymptotic analysis of Busse (1968), our generalized model, and our reduced model. The fundamental differences between all three models are twofold. First, the model of Busse (1968) and Noir *et al.* (2003) uses an approximate form of the inviscid part of the equations, valid only for small departure from the sphere ($1-\gamma \ll 1$) and for small $Po \ll 1$; while the generalized and reduced models use an exact derivation for the inviscid part. Second, all three models are based on a different derivation of the viscous torque: Busse (1968) and Noir *et al.* (2003) are based on the asymptotic values of $\lambda^{i,r}_{so}$ of the sphere and on the no-spin-up condition; the generalized model uses the asymptotic values of $\lambda^{i,r}_{so}$ for an oblate spheroid of arbitrary

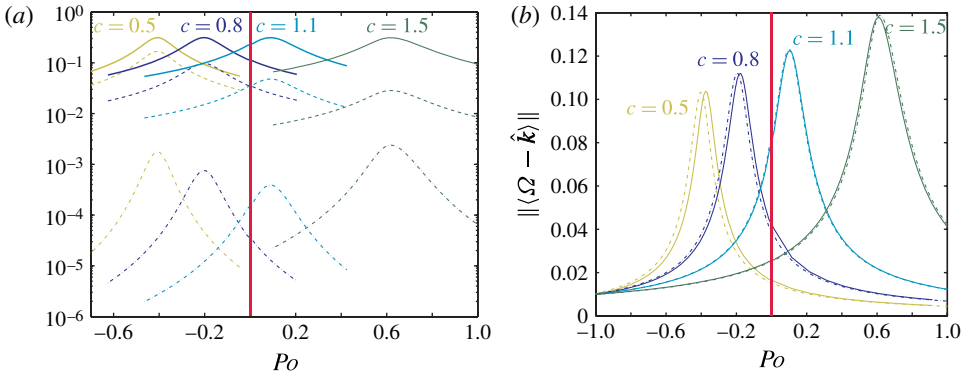

FIGURE 14. (Colour online) (*a*) Amplitude of the viscous terms in the generalized model associated with λ^r, λ^i and λ_{sup} (A 8)–(A 11). The greyscale (colour online) scheme stands for the different polar flattenings, as indicated; the solid, dashed and dot-dashed lines represent the contributions from the λ^r, λ^i_{so} and λ_{sup} terms, respectively. (*b*) Comparison of the equatorial component of rotation between the generalized model (dot-dashed lines) and the reduced model (solid lines). In both models we use $a = b = 1$, $c = 0.5,\ 0.8,\ 1.1,\ 1.5$, $E = 10^{-3}$, $Ro = 10^{-2}$ and the values of λ^r and λ^i of Zhang *et al.* (2004). The vertical line symbolizes the region of the parameter space $|Po| < 10^{-2}$ where no α can satisfy $Ro = Po \sin\alpha$.

ellipticity from Zhang *et al.* (2004) and does not impose the no-spin-up condition; and finally the reduced model neglects the terms proportional to λ^i_{so} and λ_{sup} and we thus have to close by fitting the best value of λ^r_{so}.

Figure 14(*a*) shows the contribution of the different terms of the viscous torque in the generalized model (A 8)–(A 11). We observe that, throughout the entire range of Po and for all geometries, the terms proportional to λ_{sup} (due to the axial differential rotation) remain 2–3 orders of magnitude smaller than the term proportional to λ^r_{so} and can therefore be neglected. The contribution from the term proportional to λ^i_{so} remains 4–20 times smaller than the term proportional to λ^r_{so}. Although not negligible, this term is expected to have a limited effect on the dynamics of the uniform vorticity flow. In most of our simulations, the generalized model thus reduces to the reduced model. This is illustrated in figure 14(*b*), which compares, for the axisymmetric spheroids considered in this study, the generalized and reduced models with the same value of λ^r_{so}. We observe a small shift in the locations of the peaks, which reflects the absence of the correction in λ^i_{so} in the reduced model. In agreement with figure 14(*a*), this shift is larger for $c = 0.5$, where both the λ^r_{so} and λ^i_{so} contributions are of the same order.

We now compare the generalized model and reduced models with $\lambda = \lambda^r_{so} = -3.03$ (Zhang *et al.* 2004) to the asymptotic solution of Busse (1968) and Noir *et al.* (2003) using both the asymptotic value $\lambda = \lambda^r_{so} = -2.62$ (Greenspan 1968) and the asymptotic value $\lambda = \lambda^r_{so} = -3.03$ (Zhang *et al.* 2004) (figure 15). In addition, we represent the Po_c for the classical inviscid of Poincaré obtained by substituting $\mathscr{L}\boldsymbol{\Gamma}_v = 0$ in (A 14)–(A 16) and assuming a stationary solution. It illustrates that the location of the peak is determined primarily by the inviscid form of the equations, which are exact in our model and approximated for small Po and small ellipticity in Busse (1968) and Noir *et al.* (2003). Meanwhile, as seen from our reduced model, the variation in λ^i_{so} contributes to a small detuning of the peak but the amplitude is mostly determined by the decay rate λ^r_{so}.

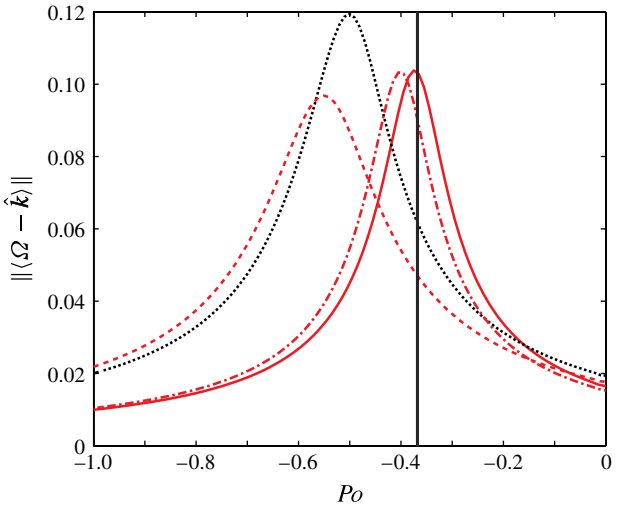

FIGURE 15. (Colour online) Norm of the differential rotation for $a = b = 1$, $c = 0.5$, $E = 10^{-3}$ and $Ro = 10^{-2}$. The solid lines represent the reduced model, the dashed line represents the asymptotic theory of Busse (1968) and Noir *et al.* (2003), and the dot-dashed line represents the generalized model. The greyscale (colour online) scheme stands for the different values of $\lambda_{so}^{r,i}$ from Greenspan (1968) (black dotted) and from Zhang *et al.* (2004) (all other strokes; red online). The vertical line represents the critical *Po* predicted from a purely inviscid model.

This validates the use of the reduced model in the case of an axisymmetric spheroid, and we are confident that the same general remarks apply to the case of a non-axisymmetric container.

REFERENCES

ABRAMOWITZ, M. & STEGUN, I. 1972 *Handbook of Mathematical Functions*. Dover.

AGRAWAL, B. N. 1993 Dynamic characteristics of liquid motion in partially filled tanks of a spinning spacecraft. *J. Guid. Control Dyn.* **16** (4), 636–640.

BAO, G. W. & PASCAL, M. 1997 Stability of a spinning liquid-filled spacecraft. *Arch. Appl. Mech.* **67** (6), 407–421.

BAYLY, B. J. 1986 Three-dimensional instability of elliptical flow. *Phys. Rev. Lett.* **57** (17), 2160–2163.

BOISSON, J., CÉBRON, D., MOISY, F. & CORTET, P. P. 2012 Earth rotation prevents exact solid body rotation of fluids in the laboratory. *Europhys. Lett.* **98**, 59002.

BONDI, H. & LYTTLETON, R. A. 1953 On the dynamic theory of the rotation of the Earth: the effect of precession on the motion of the liquid core. *Proc. Camb. Phil. Soc* **49**, 498–515.

BULLARD, E. C. 1949 The magnetic flux within the Earth. *Proc. R. Soc. Lond.* A **197**, 433–453.

BUSSE, F. H. 1968 Steady fluid flow in a precessing spheroidal shell. *J. Fluid Mech.* **33** (4), 739–751.

CÉBRON, D., LE BARS, M., LEONTINI, J., MAUBERT, P. & LE GAL, P. 2010*a* A systematic numerical study of the tidal instability in a rotating triaxial ellipsoid. *Phys. Earth Planet. Inter.* **182**, 119–128.

CÉBRON, D., LE BARS, M. & MEUNIER, P. 2010*b* Tilt-over mode in a precessing triaxial ellipsoid. *Phys. Fluids* **22**, 116601.

DWYER, C. A., STEVENSON, D. J. & NIMMO, F. 2011 A long-lived lunar dynamo driven by continuous mechanical stirring. *Nature* **479**, 212–214.

FALLER, A. J. 1991 Instability and transition of disturbed flow over a rotating disk. *J. Fluid Mech.* **230**, 245–269.

GANS, R. F. 1984 Dynamics of a near-resonant fluid-filled gyroscope. *AIAA J.* **22** (10), 1465–1471.

GARG, S. C., FURUMOTO, N. & VANYO, J. P. 1986 Spacecraft nutational instability prediction by energy-dissipation measurements. *J. Guid. Control Dyn.* **9**, 357–362.

GLAMPEDAKIS, K., ANDERSSON, N. & JONES, D. I. 2009 Do superfluid instabilities prevent neutron star precession? *Mon. Not. R. Astron. Soc.* **394**, 1908–1924.

GOLDREICH, P. 1967 Precession of the moon's core. *J. Geophys. Res.* **72** (12), 3135–3137.

GOTO, S., ISHII, N., KIDA, S. & NISHIOKA, M. 2007 Turbulence generator using a precessing sphere. *Phys. Fluids* **19**, 061705.

GREENSPAN, H. P. 1968 *The Theory of Rotating Fluids*. Cambridge University Press.

GREENSPAN, H. P. & HOWARD, L. N. 1963 On a time-dependent motion of a rotating fluid. *J. Fluid Mech.* **17** (3), 385–404.

GREFF-LEFFTZ, M. & LEGROS, H. 1999 Core rotational dynamics and geological events. *Science* **286** (5445), 1707–1709.

HINDMARSH, A. C., BROWN, P. N., GRANT, K. E., LEE, S. L., SERBAN, R., SHUMAKER, D. E. & WOODWARD, C. S. 2005 SUNDIALS: suite of nonlinear and differential/algebraic equation solvers. *ACM Trans. Math. Softw.* **31** (3), 363–396.

HOUGH, S. S. 1895 The oscillations of a rotating ellipsoidal shell containing fluid. *Phil. Trans. R. Soc. Lond.* A **186**, 469–506.

KERSWELL, R. R. 1993 The instability of precessing flow. *Geophys. Astrophys. Fluid Dyn.* **72** (1), 107–144.

KERSWELL, R. R. 1996 Upper bounds on the energy dissipation in turbulent precession. *J. Fluid Mech.* **321**, 335–370.

KIDA, S. 2011 Steady flow in a rapidly rotating sphere with weak precession. *J. Fluid Mech.* **680**, 150–193.

KIDA, S. & NAKAZAWA, N. 2010 Super-rotation flow in a precessing sphere. *Theor. Comput. Fluid Dyn.* **24** (1–4), 259–263.

LACAZE, L., LE GAL, P. & LE DIZÈS, S. 2004 Elliptical instability in a rotating spheroid. *J. Fluid Mech.* **505**, 1–22.

LAGRANGE, R., ELOY, C., NADAL, F. & MEUNIER, P. 2008 Instability of a fluid inside a precessing cylinder. *Phys. Fluids* **20**, 081701.

LAGRANGE, R., MEUNIER, P., NADAL, F. & ELOY, C. 2011 Precessional instability of a fluid cylinder. *J. Fluid Mech.* **666**, 104–145.

LE BARS, M., LACAZE, L., LE DIZÈS, S., LE GAL, P. & RIEUTORD, M. 2010 Tidal instability in stellar and planetary binary systems. *Phys. Earth Planet. Inter.* **178** (1–2), 48–55.

LE BARS, M., WIECZOREK, M. A., KARATEKIN, Ö. , CÉBRON, D. & LANEUVILLE, M. 2011 An impact-driven dynamo for the early moon. *Nature* **479**, 215–218.

LE DIZÈS, S. 2000 Three-dimensional instability of a multipolar vortex in a rotating flow. *Phys. Fluids* **12**, 2762–2774.

LINGWOOD, R. J. 1997 Absolute instability of the Ekman layer and related rotating flows. *J. Fluid Mech.* **331**, 405–428.

LORENZANI, S. 2001 Fluid instabilities in precessing ellipsoidal shells. PhD thesis, Niedersächsische Staats- und Universitätsbibliothek Göttingen.

LORENZANI, S. & TILGNER, A. 2001 Fluid instabilities in precessing spheroidal cavities. *J. Fluid Mech.* **447**, 111–128.

LORENZANI, S. & TILGNER, A. 2003 Inertial instabilities of fluid flow in precessing spheroidal shells. *J. Fluid Mech.* **492**, 363–379.

MALKUS, W. V. R. 1968 Precession of the Earth as the cause of geomagnetism: experiments lend support to the proposal that precessional torques drive the Earth's dynamo. *Science* **160** (3825), 259–264.

MEUNIER, P., ELOY, C., LAGRANGE, R. & NADAL, F. C. O. 2008 A rotating fluid cylinder subject to weak precession. *J. Fluid Mech.* **599**, 405–440.

MEYER, J. & WISDOM, J. 2011 Precession of the lunar core. *Icarus* **211**, 921–924.

NOIR, J., CARDIN, P., JAULT, D. & MASSON, J.-P. 2003 Experimental evidence of nonlinear resonance effects between retrograde precession and the tilt-over mode within a spheroid. *Geophys. J. Intl* **154** (2), 407–416.

NOIR, J., JAULT, D. & CARDIN, P. 2001 Numerical study of the motions within a slowly precessing sphere at low Ekman number. *J. Fluid Mech.* **437**, 283–299.

NORE, C., LÉORAT, J., GUERMOND, J. L. & LUDDENS, F. 2011 Nonlinear dynamo action in a precessing cylindrical container. *Phys. Rev.* E **84** (1), 016317.

PAIS, M. A. & LE MOUËL, J. L. 2001 Precession-induced flows in liquid-filled containers and in the Earth's core. *Geophys. J. Intl* **144** (3), 539–554.

POINCARÉ, H 1910 Sur la précéssion des corps déformables. *Bull. Astronomique* **XXVIII**, 1–36.

SLOUDSKY, T. 1895 De la rotation de la Terre supposée fluide à son intérieur. *Bulletin de la Société Impériale des Naturalistes de Moscou, Moscou, 1895*, Vol. 2.

STEWARTSON, K. 1959 On the stability of a spinning top containing liquid. *J. Fluid Mech.* **5** (4), 577–592.

STEWARTSON, K. & ROBERTS, P. H. 1963 On the motion of liquid in a spheroidal cavity of a precessing rigid body. *J. Fluid Mech.* **17** (1), 1–20.

TILGNER, A 1998 On models of precession driven core flow. *Stud. Geophys. Geod.* **42** (3), 232–238.

TILGNER, A. 1999 Magnetohydrodynamic flow in precessing spherical shells. *J. Fluid Mech.* **379**, 303–318.

TILGNER, A. 2005 Precession driven dynamos. *Phys. Fluids* **17**, 034104.

TILGNER, A. 2007 Kinematic dynamos with precession driven flow in a sphere. *Geophys. Astrophys. Fluid Dyn.* **101** (1), 1–9.

TILGNER, A. & BUSSE, F. H. 2001 Fluid flows in precessing spherical shells. *J. Fluid Mech.* **426**, 387–396.

TRIANA, S. A., ZIMMERMAN, D. S. & LATHROP, D. P. 2012 Precessional states in a laboratory model of the Earth's core. *J. Geophys. Res.* **117** (B4), XXX–XXX.

VANYO, J. P. 1991 A geodynamo powered by luni-solar precession. *Geophys. Astrophys. Fluid Dyn.* **59** (1), 209–234.

VANYO, J., WILDE, P., CARDIN, P. & OLSON, P. 1995 Experiments on precessing flows in the Earth's liquid core. *Geophys. J. Intl* **121** (1), 136–142.

WALEFFE, F. 1990 On the three-dimensional instability of strained vortices. *Phys. Fluids* A: *Fluid Dyn.* **2**, 76–80.

WU, C. C. & ROBERTS, P. H. 2009 On a dynamo driven by topographic precession. *Geophys. Astrophys. Fluid Dyn.* **103** (6), 467–501.

ZHANG, K., CHAN, K. H. & LIAO, X. 2010 On fluid flows in precessing spheres in the mantle frame of reference. *Phys. Fluids* **22**, 116604.

ZHANG, K., LIAO, X. & EARNSHAW, P. 2004 On inertial waves and oscillations in a rapidly rotating spheroid. *J. Fluid Mech.* **504**, 1–40.